coatings

MDPI

Article

Impact of Nonlinear Thermal Radiation and Entropy Optimization Coatings with Hybrid Nanoliquid Flow Past a Curved Stretched Surface

Dianchen Lu [1], Muhammad Ramzan [2,3,*], Shafiq Ahmad [4], Ahmad Shafee [5] and Muhammad Suleman [1]

1 Department of Mathematics, Faculty of Science, Jiangsu University, Zhenjiang 212013, China; dclu@ujs.edu.cn (D.L.); suleman@ujs.edu.cn (M.S.)
2 Department of Computer Science, Bahria University, Islamabad Campus, Islamabad 44000, Pakistan
3 Department of Mechanical Engineering, Sejong University, Seoul 143-747, Korea
4 Department of Mathematics, Quaid-i-Azam University, Islamabad 44000, Pakistan; ashafiq@math.qau.edu.pk
5 Department of Applied Science, College of Technological Studies, Public Authority of Applied Education and Training, Shuwaikh Campus, Shuwaikh 70654, Kuwait; as.zada@paaet.edu.kw
* Correspondence: mramzan@bahria.edu.pk; Tel.: +92-300-512-2700

Received: 19 September 2018; Accepted: 21 November 2018; Published: 27 November 2018



Abstract: The present investigation addresses the flow of hybrid (nickel–zinc ferrite and ethylene glycol) nanoliquid with entropy optimization and nonlinear thermal radiation coatings past a curved stretching surface. Analysis was carried out in the presence of magnetohydrodynamic, heat generation/absorption, and convective heat and mass flux conditions. Solution of the modeled problem was attained numerically using MATLAB built-in function bvp4c. Impacts of prominent parameters on betrothed distributions were depicted through graphs and were well supported by requisite discussions. Numerically calculated values of Sherwood number were established in a tabulated form and were scrutinized critically. An excellent concurrence was achieved when results of the presented model were compared with previously published result; hence, dependable results are being presented. It was observed that concentration field diminished with increasing values of curvature parameter, though the opposite trend was noticed for velocity and temperature distributions. Further, it was detected that Nusselt number decreased with augmented values of radiation and curvature parameters.

Keywords: coatings; curved stretched surface; nanoliquid; nonlinear thermal radiation; entropy generation

1. Introduction

Numerous applications of heat transfer liquids or coolants can be found in a variety of fields, such as automobiles, industry, electronics, and cooling processes. In all such industrial applications, cooling by liquids has been used for years. The process of cooling by fluids may be the single phase (where there is no phase change in the coolant) or two-phase (where coolant liquid will experience a phase change). In the latter, latent heat influences the cooling efficiency [1]. Several coolants, such as water, ethylene glycol, blend of water and glycol, propylene glycol and amalgamation of water, and propylene glycol, are used as coolants in automobiles and industrial cooling processes. In the last two decades, several researchers have devoted their efforts to increasing thermal conductivity of coolants, thereby improving heat transfer capabilities. The pioneering work of Choi et al. [2] introduced nanofluids by insertion of solid nanoparticles into liquids, thus enhancing the thermal properties of these liquids.

This pioneering work has remarkably revolutionized modern engineering and the industrial world. Nanofluids are an amalgamation of suspended solid material particles and customary liquids (ethylene glycol, water). This new type of advanced material possesses amazing capabilities that trigger the process of heat transfer and augments the thermal conductivity of the base fluid. Enhancement in the thermal conductivity and heat transfer is visualized once ferrite nanoparticles are added into the base liquid. Several examples featuring heat transfer can be quoted, including chemicals, cooling and heating system of buildings, and avionics cooling systems. Nanofluids exhibit potentially exceptional features in comparison to macrometer-sized particles. This is because nanoparticles have sufficiently larger surface area compared to micrometer-sized particles; this is the reason nanofluids possess incomparable capabilities of heat transfer [3].

In several electromagnetic applications with high permeability, e.g., electromagnetic wave absorbers and inductors, usage of nickel–zinc ferrite can be noticed. To minimize energy losses related to bulk powders, usage of nickel–zinc nanoparticles has been recommended by a number of researchers [4–6]. In addition, a majority of electronic gadgets require such materials to be compressed into outsized shapes with the required thickness, which is reasonably challenging if the size of these particles is large enough. Several methods have been proposed to get nickel–zinc ferrite, including ball milling, precipitation, and hydrothermal. Ferrofluids are colloidal fluids comprising ferromagnetic or ferrimagnetic nanoparticles suspended in an electrically insulated hauler fluid. In the current examination, ethylene glycol ($C_2H_6O_2$) was taken as a carrier fluid. The assumed ferrite nanoparticle was nickel–zinc ferrite ($NiZnFe_2O_4$) crystallize in the normal spinal structure. Typically, at room temperature, the inverted spinals are ferromagnetic and normal spinals are paramagnetic. Moreover, zinc ferrites act like antiferromagnetic in nature at low temperature. This feature makes ferromagnetic nanofluids more relevant in different real-world applications [7,8]. The ferrofluid's flow with the effect of thermal gradients and the magnetic field was discussed by Neuringer [9]. Majeed et al. [10] demonstrated the heat transfer investigation in a ferromagnetic fluid flow.

The subject of fluid flow past stretched surfaces has diverse engineering and industrial applications, including paper production, glass blowing, crystal growing, hot rolling, manufacturing of rubber sheets, annealing of copper wires, etc. The coined work of Crane [11] discussing the flow past a linearly stretching surface urged fellow researchers to discover more avenues in this exciting and interesting subject. This was followed by the remarkable work of Gupta and Gupta [12] who pondered on the flow past a spongy surface. Then, Chakrabarti and Gupta [13] examined the hydromagnetic flow past a stretched surface. Andersson et al. [14] considered the flow of power-law fluid past a surface, which was linearly stretched under the influence of magnetic forces. The flow of an Oldroyd-B fluid with the impact of generation/absorption was deliberated by Hayat et al. [15]. Muhammad et al. [16] discussed the effect of thermal stratification in the ferromagnetic fluid on a stretching sheet. Ramzan and Yousaf [17] demonstrated that the elastic viscous nanofluid finished a bi-directional stretching surface in view of Newtonian heating. Hussain et al. [18] utilized the exponentially stretching sheet to scrutinize the flow of Jeffrey nanofluid with radiation effects. Some recent explorations highlighting various fluid flows past stretched surfaces with coatings can be found in references [19–22].

In today's cutting-edge engineering technology, curved stretching has a broad relevance because of its different uses in industry, for example, in transportation and electronics. Sanni et al. [23] attained a numerical solution for the viscous fluid flow on a curved stretched channel. Sajid et al. [24] inspected the ferrofluid (Fe_3O_4) flow on a curved sheet with effects of Joule heating and magnetic forces. Rosca and Pop [25] studied time-dependent flow along a spongy curved surface. Imtiaz et al. [26] introduced the effect of homogeneous/heterogeneous reactions in ferrofluid embedded in a stretching surface. Naveed et al. [27] calculated heat transfer and used the micropolar fluid to analyze the effects over a curved surface with thermal radiation.

A literature review has specified that copious studies are available relating to nanofluids with linear/nonlinear/exponential stretching surfaces but comparatively less research work is available highlighting curved stretched surfaces. This gets even narrower when we talk about the study of hybrid

nanoliquid with entropy optimization past curved surfaces. Therefore, our task here is to discuss hybrid nanoliquid flow comprising ferromagnetic nanoparticle, i.e., nickel–zinc ferrite ($NiZnFe_2O_4$), and the base fluid, i.e., ethylene glycol ($C_2H_6O_2$), over a curved surface with entropy optimization coating. The whole analysis was performed with added impressions of nonlinear thermal radiation with entropy optimization coatings. The analysis was supported by the convective heat and mass flux boundary conditions. Numerical solution of the envisioned model was obtained by utilizing bvp4c from MATLAB. The traits of the sundry parameters on involved distributions were thoroughly discussed keeping their physical justification in mind.

2. Mathematical Formulation

We considered a 2D steady, incompressible nanoliquid flow over a curved stretching channel looped in the form of a circle with a radius R about the curvilinear directions r and x, as shown in Figure 1. Here, a higher value of R corresponds to a marginally curved surface. The stretching velocity is taken as $u = u_w$ along the x-direction. A magnetic field is applied normal to the fluid flow and along the r-direction. The electric and induced magnetic fields were overlooked owing to our assumption of small Reynolds number.

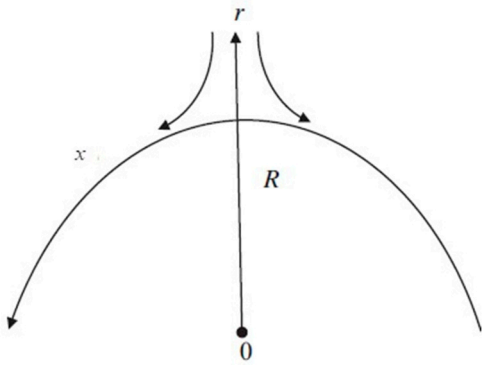

Figure 1. Flow geometry.

The assumed system is governed by the following equations:

$$\frac{\partial}{\partial r}\{(R+r)v\} + R\frac{\partial u}{\partial x} = 0 \tag{1}$$

$$\frac{u^2}{r+R} = \frac{1}{\rho_{nf}}\frac{\partial p}{\partial r} \tag{2}$$

$$v\frac{\partial u}{\partial r} + \frac{Ru}{r+R}\frac{\partial u}{\partial x} + \frac{uv}{r+R} = -\frac{1}{\rho_{nf}}\frac{R}{r+R}\frac{\partial p}{\partial x} + \frac{\mu_{nf}}{\rho_{nf}}\left(\frac{\partial^2 u}{\partial r^2} + \frac{1}{r+R}\frac{\partial u}{\partial r} - \frac{u}{(r+R)^2}\right) - \frac{\sigma}{\rho_{nf}}{B_0}^2 u \tag{3}$$

$$v\frac{\partial T}{\partial r} + \frac{Ru}{r+R}\frac{\partial T}{\partial x} = \alpha_{nf}\left(\frac{\partial^2 T}{\partial r^2} + \frac{1}{r+R}\frac{\partial T}{\partial r}\right) + \frac{Q_0}{(\rho C_p)_{nf}}(T_\infty - T) + \frac{1}{(\rho C_p)_{nf}}\frac{1}{r+R}\frac{\partial}{\partial r}(r+R)q_r \tag{4}$$

$$v\frac{\partial C}{\partial r} + \frac{Ru}{r+R}\frac{\partial C}{\partial x} = D_B\left(\frac{\partial^2 C}{\partial r^2} + \frac{1}{r+R}\frac{\partial C}{\partial r}\right) \tag{5}$$

The system of Equations (1)–(5) is supported by the following boundary conditions:

$$\begin{gathered} v|_{r=0} = 0,\ u|_{r=0} = u_w(x) = sx,\ k_f\frac{\partial T}{\partial r}\Big|_{y=0} = h^*(T_f - T),\ -D_B\frac{\partial C}{\partial r}\Big|_{r=0} = j_w \\ u|_{r\to\infty} \to 0,\ \frac{\partial u}{\partial r}\Big|_{r\to\infty} \to 0,\ T|_{r\to\infty} \to T_\infty,\ C|_{r\to\infty} \to C_\infty \end{gathered} \tag{6}$$

The thermophysical traits of the hybrid nanoliquid are appended in Table 1.

Table 1. The values of C_p, ρ, and k for ethylene glycol and $NiZnFe_2O_4$ (nickel–zinc ferrite) [28–33].

Thermo-Physical Characteristics of the Ethylene Glycol and Nickel–Zinc Ferrite	C_p (J/kg K)	ρ (kg/m^3)	k (W/mK)	Pr
ethylene glycol($C_2H_6O_2$)	2382.0	1116.6	0.2490	204.0
nickel–zinc ferrite($NiZnFe_2O_4$)	710.0	4800.0	6.3	–

The mathematical form of thermophysical properties are given as follows:

$$\mu_{nf} = \frac{\mu_f}{(1-\phi)^{2.5}},\ \alpha_{nf} = \frac{k_{nf}}{(\rho C_p)_{nf}} \tag{7}$$

$$\rho_{nf} = (1-\phi)\rho_f + \phi\rho_s,\ (\rho C_p)_{nf} = (1-\phi)(\rho C_p)_f + \phi(\rho C_p)_s \tag{8}$$

$$\frac{k_{nf}}{k_f} = \frac{(k_s+2k_f) - 2\phi(k_f-k_s)}{(k_s+2k_f) + \phi(k_f-k_s)} \tag{9}$$

In Equation (4), the nonlinear radiation heat flux term via Rosseland's approximation is given as follows:

$$q_r = \frac{4\sigma^*}{3k^*}\frac{\partial T^4}{\partial r} = \frac{16\sigma^* T^3}{3k^*}\frac{\partial T}{\partial r} \tag{10}$$

3. Solution Procedure

Here, we used the following dimensionless transformations:

$$\begin{gathered}\zeta = \sqrt{\tfrac{s}{\nu_f}}r,\ p = \rho_f s^2 x^2 P(\zeta),\ T = T_\infty(1+(\theta_w-1)\theta),\\ C = C_\infty + \tfrac{j_w}{D_B}\sqrt{\tfrac{\nu_f}{s}}h(\zeta),\ u = sxf'(\zeta),\ v = -\tfrac{R}{r+R}\sqrt{s\nu_f}f(\zeta)\end{gathered} \tag{11}$$

Here, prime denotes the derivative w, r, T, ζ and $\theta_w = T_f/T_\infty$. The above transformation Equation (11) satisfies Equation (1) identically and Equations (2)–(6) are given by the following:

$$P' = \left(1-\phi+\phi\frac{\rho_s}{\rho_f}\right)\frac{f'^2}{\zeta+K_1} \tag{12}$$

$$\begin{aligned}\frac{1}{\left(1-\phi+\phi\frac{\rho_s}{\rho_f}\right)}\frac{2K_1}{\zeta+K_1}P = {}& \frac{1}{(1-\phi)^{25/10}\left(1-\phi+\phi\frac{\rho_s}{\rho_f}\right)}\left(f''' - \frac{f'}{(K_1+\zeta)^2} + \frac{f''}{\zeta+K_1}\right) - \frac{K_1}{\zeta+K_1}f'^2\\ & + \frac{K_1}{K_1+\zeta}ff'' + \frac{K_1}{(K_1+\zeta)^2}f'f - Mf'\end{aligned} \tag{13}$$

$$\begin{aligned}&\frac{1}{\Pr}\left(\frac{k_{nf}}{k_f} + R_d(1+(\theta_w-1)\theta)^3\right)\left(\theta'' + \frac{1}{\zeta+K_1}\theta'\right) + \left(1-\phi+\phi\frac{(\rho C_p)_s}{(\rho C_p)_f}\right)\left(\frac{K_1}{\zeta+K_1}f\theta'\right)\\ &\lambda_1\theta + 3R_d(1+(\theta_w-1)\theta)^2\theta' = 0\end{aligned} \tag{14}$$

$$h'' + \frac{1}{\zeta+K_1}h' + S_c\left(\frac{K_1}{\zeta+K_1}\right)fh' = 0 \tag{15}$$

and

$$\begin{gathered}f(\zeta) = 0,\ f'(\zeta) = 1,\ \theta'(\zeta) = (1-\theta(\zeta))\mathrm{Bi},\ h'(\zeta) = -1,\ \text{as } \zeta = 0\\ f'(\zeta)\to 0,\ f''(\zeta)\to 0,\ \theta(\zeta)\to 0,\ h(\zeta)\to 0,\ \text{as } \zeta\to\infty\end{gathered} \tag{16}$$

Here, $K_1 = R\sqrt{\frac{s}{\nu_f}}$, $\mathrm{Bi} = \frac{h^*\sqrt{\frac{\nu_f}{s}}}{k_f}$, $S_c = \frac{\nu_f}{D_B}$, $R_d = \frac{16\sigma^* T_\infty{}^3}{3kk^*}$, $\lambda_1 = \frac{Q_0}{s(\rho C_p)_f}$, and $\Pr = \frac{\nu_f}{\alpha_f}$.

Eliminating pressure term from Equations (12) and (13) by differentiating Equation (13) with respect to ζ and then putting in Equation (12), we get the following:

$$f^{iv} + \frac{2f'''}{\zeta+K_1} - \frac{f''}{(\zeta+K_1)^2} + \frac{f'}{(\zeta+K_1)^3} + (1-\phi)^{25/10}\left(1-\phi+\phi\frac{\rho_s}{\rho_f}\right)\{\frac{K_1}{(\zeta+K_1)^2}(f'^2 - ff'') - \frac{K_1}{\zeta+K_1}(f'f'' - ff''') - \frac{K_1}{(\zeta+K_1)^3}ff'\} - (1-\phi)^{25/10}M(\frac{f'}{\zeta+K_1} + f'') = 0 \quad (17)$$

with

$$f(0) = 0,\ f'(0) = 1,\ f'(\infty) \to 0,\ f''(\infty) \to 0 \quad (18)$$

The surface drag force (C_f), Sherwood number (Sh_x), and Nu_x (Nusselt number) along x-direction are defined as follows:

$$C_f = \frac{\tau_{rx}}{\frac{1}{2}\rho u_w^2},\ \mathrm{Nu}_x = \frac{xq_w}{k_f(T_f - T_\infty)},\ \mathrm{Sh}_x = -\frac{x}{(C-C_\infty)}\frac{\partial C}{\partial r} \quad (19)$$

where

$$\tau_{rx} = \mu_{nf}(\frac{\partial u}{\partial r} - \frac{u}{r+R})_{r=0}, q_w = (q_r)_w - (\frac{\partial T}{\partial r})_{r=0} \quad (20)$$

After putting Equations (11) and (20), Equation (19) becomes the following:

$$\frac{1}{2}C_f(\mathrm{Re}_x)^{\frac{1}{2}} = f''(0) - \frac{f'(0)}{K_1},\ \mathrm{Nu}_x(\mathrm{Re}_x)^{-\frac{1}{2}} = -\left[\frac{k_{nf}}{k_f} + R_d(1+(\theta_w-1)\theta(0))^3\right]\theta'(0),\ \mathrm{Sh}_x(\mathrm{Re}_x)^{-\frac{1}{2}} = \frac{1}{h(0)} \quad (21)$$

Here, $\mathrm{Re}_x = \frac{sx^2}{v_f}$.

4. Entropy Generation

The equation of entropy generation in dimensional form is given in reference [34].

$$E_{gen}''' = \frac{k_{nf}}{T_f^2}\left[\left(\frac{\partial T}{\partial r}\right)^2 + \frac{16\sigma^* T^3}{3k_{nf}k^*}\left(\frac{\partial T}{\partial y}\right)^2\right] + \frac{\mu_{nf}}{T_f}\left(\frac{\partial u}{\partial r}\right)^2 + \frac{\sigma B^2{}_0}{T_f}u^2 + \frac{RD}{C_\infty}\left(\frac{\partial C}{\partial r}\right)^2 + \frac{RD}{T_f}\left(\frac{\partial C}{\partial r}\right)\left(\frac{\partial T}{\partial r}\right) \quad (22)$$

Equation (22) after applying the requisite transformations takes the following form:

$$N_G = \frac{E_{gen}'''}{E_0'''} = \mathrm{Re}_x\left[\frac{k_{nf}}{k_f} + R_d(1+\Pi\theta)^3\right]\theta'^2 + \frac{\mathrm{BrRe}_x}{\Pi^2}(f'')^2 + \frac{\mathrm{BrRe}_x}{\Pi^2}Mf'^2 + \frac{\mathrm{Re}_x\sum}{\Pi}\left(h'^2 + \frac{\theta' h'}{\Pi}\right) \quad (23)$$

where

$$\mathrm{Br} = \frac{\mu_{nf}{u_w}^2}{k_{nf}T_f},\ \mathrm{Re}_x = \frac{x^2 s}{\nu_f},\ \sum = \frac{C_\infty RD}{k_{nf}},\ \Pi = \theta_w - 1 \quad (24)$$

5. Results and Discussion

The MATLAB built-in function bvp4c was applied to integrate the numerical solution for the system of Equations (14), (15), and (17) with initial and boundary conditions, Equations (16) and (18), for numerous values of K_1, M, R_d, λ_1, and $\mathrm{S_c}$ graphically. For this technique, we first changed differential equations with the higher order to the equations of order one by utilizing new variables. The function bvp4c needs an initial guess for the solution and with the tolerance of 10^{-7}. The guess we chose needed to satisfy the boundary conditions (Equations (16) and (18)) and the solution. The validation of our presented results is depicted in Table 2. An excellent agreement with Sanni et al. [23] was observed when M = 1, φ = 0.0, and in the absence of temperature and concentration profile.

Table 2. Comparison of presented results for skin friction coefficient $\frac{1}{2}C_f(\mathrm{Re}_x)^{\frac{1}{2}}$ when $M = 1$ and $\varphi = 0.0$.

K_1	Sanni et al. [23]	Present Result
5	1.1576	1.15760
10	1.0734	1.07341
20	1.0355	1.03540
50	1.0140	1.01400
100	1.0070	1.00690
1000	1.0008	1.00079

Figures 2 and 3 show the impression of solid volume fraction φ on velocity and temperature profiles. Both velocity fields increased with increasing values of solid volume fraction φ. Further, the momentum and thickness of the thermal boundary layers were boosted with a larger value of φ. The values given to other parameters were $Pr = 10$, $S_c = 0.5$, $K_1 = 10$, $R_d = 0.5$, $\theta_w = 0.5$, $\lambda_1 = 0.5$, and $M = 0.1$.

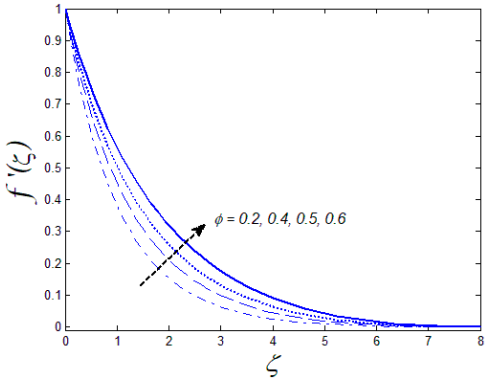

Figure 2. Upshot of φ on velocity distribution $f'(\zeta)$.

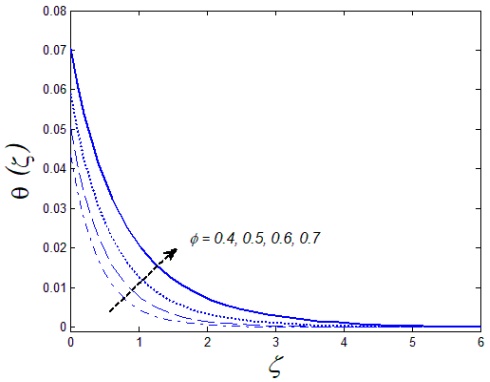

Figure 3. Upshot of φ on temperature field $\theta(\zeta)$.

The impact of the curvature parameter K_1 on velocity, concentration, and temperature profiles are depicted in Figures 4–6. Increasing values of K_1 resulted in an increase in fluid velocity and temperature field, while the concentration profile diminished. This was because of the radius of the surface augment when curvature parameter K_1 was increased. As a result, the flow increased but it offered more resistance, therefore the temperature rose. The values of other parameters were fixed as $Pr = 10$, $S_c = 0.5$, $\varphi = 0.1$, $R_d = 0.5$, $\theta_w = 0.5$, $\lambda_1 = 0.5$ and $M = 0.1$.

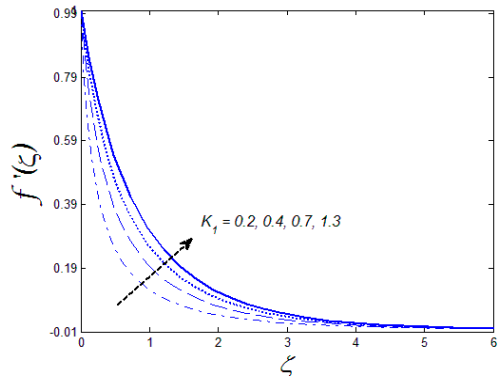

Figure 4. Upshot of K_1 on velocity profile $f'(\zeta)$.

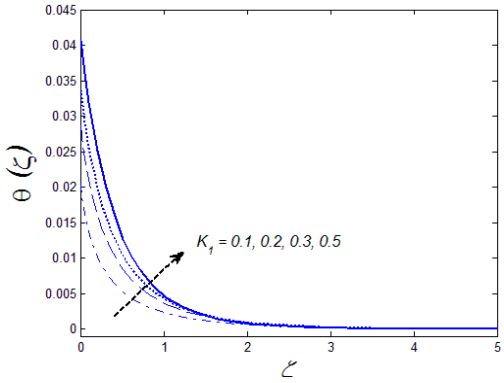

Figure 5. Upshot of K_1 on temperature profile $\theta(\zeta)$.

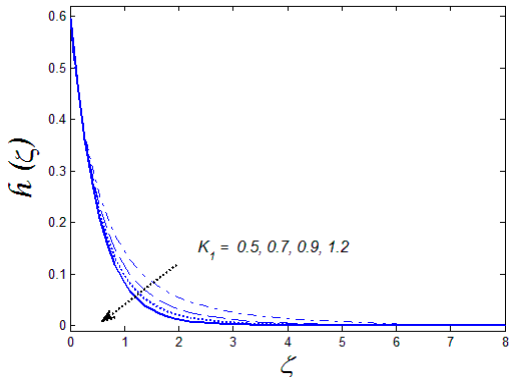

Figure 6. Upshot of K_1 on concentration field $h(\zeta)$.

Figure 7 demonstrates the variation in the velocity field for numerous estimates of magnetic parameter M. Here, increments in M led to a decline in the magnitude of fluid's velocity. This was because of the resistive force (called Lorentz force) triggered by the magnetic field, which lowered the velocity of the fluid's velocity flow. The values of the other parameters were fixed as $K_1 = 10$, $S_c = 0.5$, $\varphi = 0.1$, $R_d = 0.5$, $\theta_w = 0.5$, $\lambda_1 = 0.5$, and Bi = 0.1.

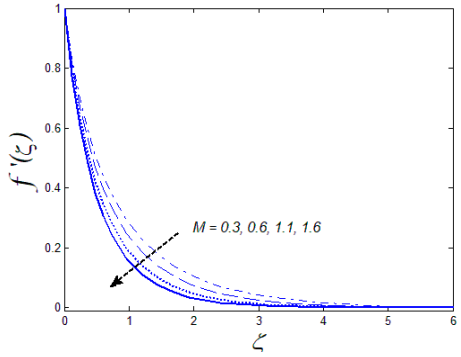

Figure 7. Upshot of M on velocity profile $f'(\zeta)$.

The characteristics of Biot number Bi and heat generation/absorption parameter λ_1 on temperature field are displayed in Figures 8 and 9, respectively. Figure 8 shows that the convective heat transfer coefficient intensified for higher estimates of Bi and the temperature subsequently rose. Figure 9 illustrates the behavior of λ_1. To increase the estimation values of heat absorption/generation parameter, the temperature profile and thermal boundary layer thickness were increased. The values of other parameters were fixed as $K_1 = 10$, $M = 0.3$, $\varphi = 0.5$, $R_d = 0.1$, $\theta_w = 0.5$, and $Pr = 10$.

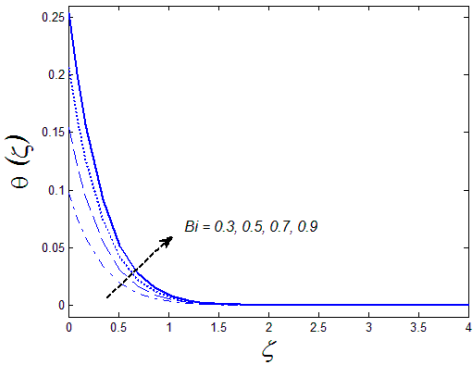

Figure 8. Upshot of Bi on temperature field $\theta(\zeta)$.

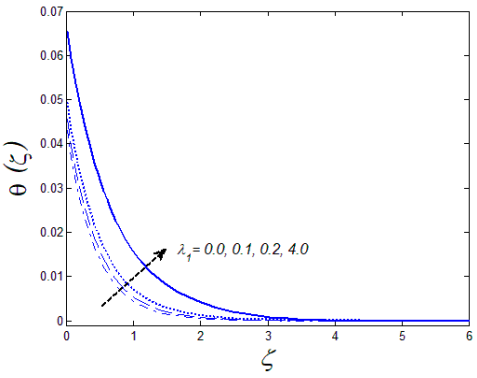

Figure 9. Upshot of λ_1 on temperature distribution $\theta(\zeta)$.

Figures 10 and 11 show the impacts of nonlinear radiation parameter R_d and Prandtl number Pr on temperature distribution, respectively. It can be seen that the temperature field fell with increasing Prandtl number Pr. As Prandtl number is linked in a reciprocal way to the thermal diffusivity, a quick augmentation in the Prandtl number Pr lessened the temperature and thickness of the thermal boundary layer. The temperature profile increased with increment in nonlinear radiation parameter R_d. Physically, the radiative heat flux increased with increasing values of R_d which ultimately boosted

the temperature of the fluid. The values assigned to other parameters were $K_1 = 10$, $M = 0.3$, $\varphi = 0.5$, Bi = 0.1, $\theta_w = 0.5$, and $S_c = 5$.

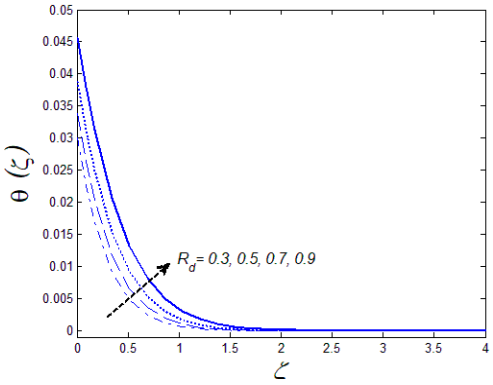

Figure 10. Upshot of R_d on temperature field θ**(ζ)**.

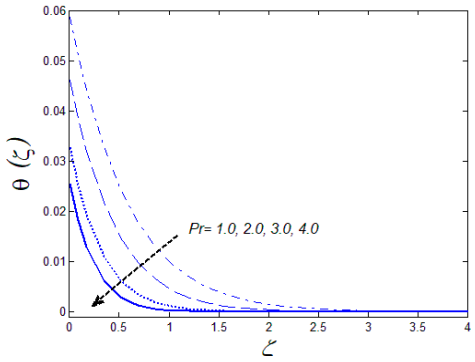

Figure 11. Upshot of Pr on temperature field θ**(ζ)**.

The impression of Schmidt number S_c on concentration distribution is portrayed in Figure 12. A decrease in concentration field was detected with increasing values of S_c. As the Schmidt number has a converse proportion with the Brownian diffusion coefficient, an increment in the S_c yielded a decay in Brownian diffusion coefficient that brought about a diminishment in concentration and its interrelated boundary layer thickness. The values allocated to other parameters were $K_1 = 10$, $M = 0.3$, $\varphi = 0.1$, Bi = 0.1, $\theta_w = 0.5$, and $R_d = 0.1$.

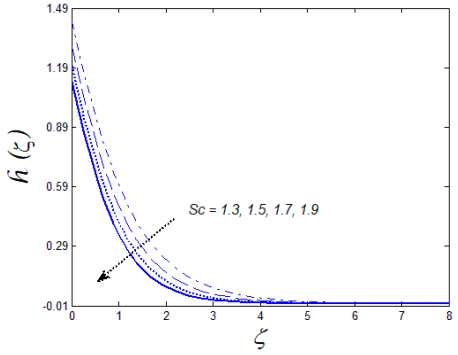

Figure 12. Upshot of S_c on concentration profile h**(ζ)**.

The influence of curvature parameter K_1 and magnetic parameter M on skin friction coefficient $-\frac{1}{2}C_f \mathrm{Re}_x^{1/2}$ is depicted in Figure 13. It can be noticed that the surface drag force diminished with increasing value of K_1. A contradictory trend was demonstrated in case of M. In Figure 14,

the consequence of magnetic parameter M and solid volume fraction φ on shear wall stress is demonstrated. The skin friction profile rose with increase in magnetic parameter M and solid volume fraction φ for fixed values of parameters Pr = 10, S_c = 0.5, R_d = 0.5, θ_w = 0.5, λ_1 = 0.5 and Bi = 0.1.

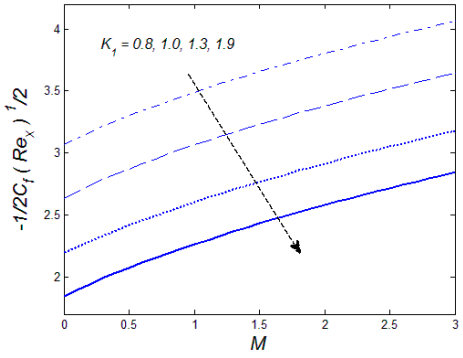

Figure 13. Upshot of K_1 and M on wall shear stress $-\frac{1}{2}C_f\mathrm{Re}_x^{1/2}$.

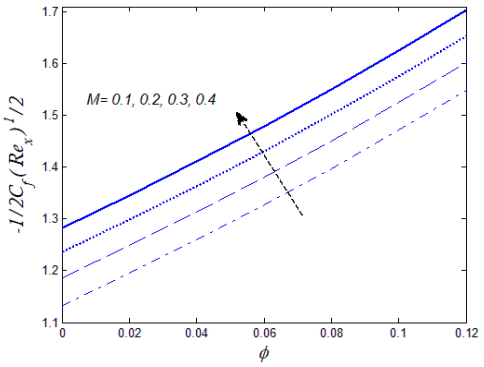

Figure 14. Upshot of M and φ on wall shear stress $-\frac{1}{2}C_f\mathrm{Re}_x^{1/2}$.

Figure 15 shows the effect of Biot number Bi and solid volume fraction φ on Nusselt number $\mathrm{Nu}_x(\mathrm{Re}_x)^{-\frac{1}{2}}$. It was detected that for higher value of Bi and φ, the surface heat transfer rate upsurged when values of parameters were given as K_1 = 10, M = 0.3, S_c = 5.0, R_d = 0.1, θ_w = 0.5, λ_1 = 0.5 and Pr = 10.

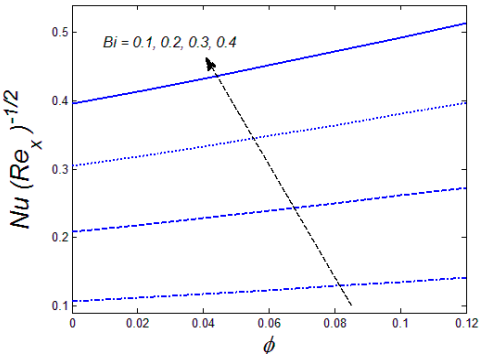

Figure 15. Upshot of Bi and on φ Nusselt number $\mathrm{NuRe}_x^{-1/2}$.

The outcome of curvature parameter K_1 and nonlinear radiation parameter R_d on Nusselt number $\mathrm{Nu}_x(\mathrm{Re}_x)^{-\frac{1}{2}}$ is examined in Figure 16. Here, a reduction in Nusselt number was noted for increasing values of curvature parameter K_1 and the opposite trend was seen for nonlinear radiation parameter R_d for fixed values of φ = 0.1, M = 0.3, S_c = 5.0, θ_w = 0.5, λ_1 = 0.5 and Pr = 10.

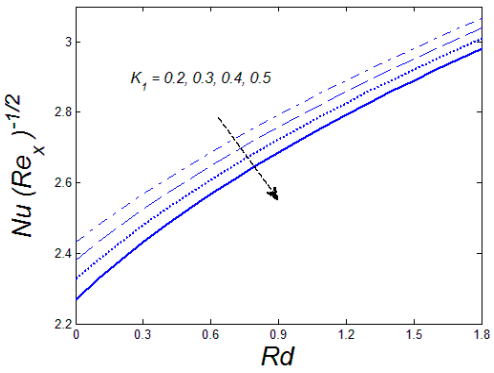

Figure 16. Upshot of K_1 and R_d on Nusselt number $\mathrm{NuRe}_x^{-1/2}$.

The impact of the Brinkman number (Br) on entropy generation is portrayed in Figure 17. From the illustration, it can be seen that entropy optimization was boosted with increasing values of (Br). The reason behind this was that more heat was generated between the layers of the fluid because of augmented values of (Br). Figure 18 displays the relationship between the magnetic parameter (M) and the entropy generation. Again, the same trait as depicted in case of (Br) was witnessed here. Higher values of (M) meant stronger Lorentz force and ultimate strengthening of the dissipation energy, and this was the main cause of irreversibility.

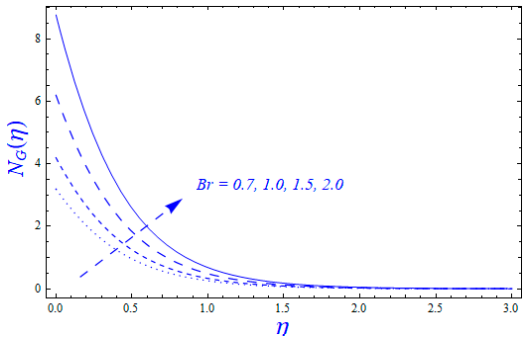

Figure 17. Upshot of Br on N_G (η).

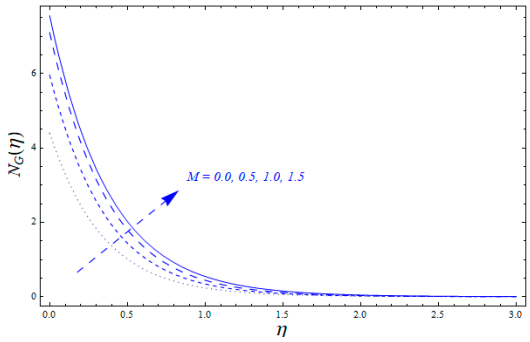

Figure 18. Upshot of M on N_G (η).

Table 3 shows the behavior of Sherwood number $\mathrm{Sh}_x(\mathrm{Re}_x)^{-\frac{1}{2}}$ for varied values of $\mathrm{S_c}$ (Schmidt number), K_1 (curvature parameter), and M (magnetic parameter). It can be seen that for snowballing values of $\mathrm{S_c}$, the Sherwood number $\mathrm{Sh}_x(\mathrm{Re}_x)^{-\frac{1}{2}}$ increased; however, it diminished for increasing value of K_1 and M.

Table 3. Numerical value of Sherwood number $\mathrm{Sh}_x(\mathrm{Re}_x)^{-\frac{1}{2}}$ for various value of parameter with fixed value of $Pr = 10$, $R_d = 0.1$, $\varphi = 0.1$, Bi = 0.1, $\theta_w = 0.5$, $\lambda_1 = 0.5\, f'(\zeta)$.

$\mathbf{S_c}$	K_1	M	$\mathbf{Sh}_x(\mathbf{Re}_x)^{-\frac{1}{2}}$
0.5	10	0.1	0.38325
1.0	–	–	0.59354
2.0	–	–	0.92268
5	5	0.1	1.60150
–	10	–	1.58090
–	50	–	1.56230
5	10	0.3	1.56270
–	–	0.5	1.54600
–	–	0.7	1.53040

6. Concluding Remarks

In this paper, the flow of nanoliquid comprising nickel–zinc ferrite–ethylene glycol ($NiZnFe_2O_4$–$C_2H_6O_2$) accompanied by entropy optimization coating past a curved stretching surface with convective heat and mass flux boundary was examined. The solution of the envisioned system of equations was found numerically by applying MATLAB built-in function bvp4c. The impact of numerous arising parameters on involved profiles was depicted via graphical illustrations with requisite discussions.

The conclusions of the current study are as follows:

- An increase in curvature parameter accounted for increasing velocity and temperature fields and diminishing concentration distribution.
- Under the considerable influence of magnetic parameter, an increased axial velocity field was attained.
- For the increasing estimates of the solid volume fraction, the temperature and velocity profiles showed increasing behavior.
- The temperature profile improved with increasing values of Biot number and heat generation/absorption parameter.
- The value of friction factor profile augmented for larger values of M and φ, but it decreased for K_1 and M.
- The Nusselt number $\mathrm{NuRe}_x^{-1/2}$ declined with increasing values of K_1 and R_d.

Author Contributions: Formal Analysis, M.R.; Funding Acquisition, D.L.; Investigation, M.R.; Methodology, D.L.; Project Administration, M.R.; Software, S.A.; Validation, M.S.; Writing—Original Draft, A.S.; Writing—Review and Editing, M.S.

Funding: This research was funded by National Natural Science Foundation China (No. 11571140 and 11671077), Faculty of Science, Jiangsu University, Zhenjiang, China.

Acknowledgments: The authors are highly thankful for exceptional support raised by the Jiangsu University, China and Bahria University, Islamabad, Pakistan.

Conflicts of Interest: Authors have no conflict of interest regarding this publication.

Nomenclature

u, v	velocity components
r, x	coordinate
R	radius of circle
P	pressure
B_0	strength of magnetic field
Q_0	volumetric rate of heat generation/absorption

q_r	nonlinear radiative heat flux
T, T_∞	temperature
C, C_w, C_∞	concentration
D_B	Brownian diffusion coefficient
T_f	convective temperature at the sheet
j_w	mass flux
u_w	stretching velocity along x-direction
k^*	mean absorption coefficient
K_1	curvature parameter
M	magnetic parameter
S	positive stretching constant
$\mathrm{S_c}$	Schmidt number
R_d	radiation parameter
h^*	convective heat transfer coefficient
C_f	surface drag force
Sh_x	Sherwood number
Re_x	local Reynolds number
E_{gen}'''	volumetric rate of local entropy generation
E_0'''	characteristic entropy generation rate
N_G	entropy generation
Br	Brinkman number
Bi	Biot number
Pr	Prandtl number
Nu_x	Nusselt number
C_s	heat capacity of surface
Greek Symbols	
ρ_{nf}, ρ_f, ρ_s	density
μ_{nf}, μ_f, μ_s	dynamic viscosity
σ	electrical conductivity
σ_{nf}	modified thermal diffusivity
$(\rho C_p)_{nf}$, $(\rho C_p)_f$	heat capacity
k_f, k_{nf}, k	thermal conductivity
φ	solid volume fraction of nanofluid
ζ	a scaled boundary-layer coordinate
σ^*	Stefan–Boltzmann constant
θ_w	temperature difference
λ_1	heat generation parameter
f	dimensionless stream function,
θ	dimensionless temperature
τ_{rx}	wall's shear stress
$\sum$	a constant parameter
α	dimensionless temperature difference
Subscripts	
w	for wall surface
nf	for the nanofluid
f	for the base fluid
s	for the solid (nanoparticles)
∞	use for ambient

References

1. Das, S.K.; Choi, S.U.; Yu, W.; Pradeep, T. *Nanofluids: Science and Technology*; John Wiley & Sons Inc.: Hoboken, NJ, USA, 2007.
2. Choi, S.U.S. Enhancing Thermal Conductivity of Fluids with Nanoparticles. In *Developments and Applications of Non-Newtonian Flows*; Singer, D.A., Wang, H.P., Eds.; ASME: New York, NY, USA, 1995; Volume 66, pp. 99–105.
3. Morrison, S.A.; Cahill, C.L.; Carpenter, E.E.; Calvin, S.; Swaminathan, R.; McHenry, M.E.; Harris, V.G. Magnetic and structural properties of nickel zinc ferrite nanoparticles synthesized at room temperature. *J. Appl. Phys.* **2004**, *95*, 6392–6395. [CrossRef]
4. Naughton, B.T.; Clarke, D.R. Lattice expansion and saturation magnetization of nickel–zinc ferrite nanoparticles prepared by aqueous precipitation. *J. Am. Ceram. Soc.* **2007**, *90*, 3541–3546. [CrossRef]
5. Virden, A.E.; O'Grady, K. Structure and magnetic properties of NiZn ferrite nanoparticles. *J. Magn. Magn. Mater.* **2005**, *290*, 868–870. [CrossRef]
6. Shahane, G.S.; Kumar, A.; Arora, M.; Pant, R.P.; Lal, K. Synthesis and characterization of Ni–Zn ferrite nanoparticles. *J. Magn. Magn. Mater.* **2010**, *322*, 1015–1019. [CrossRef]
7. Sheikholeslami, M.; Ganji, D.D.; Rashidi, M.M. Ferrofluid flow and heat transfer in a semi annulus enclosure in the presence of magnetic source considering thermal radiation. *J. Taiwan Inst. Chem. Eng.* **2015**, *47*, 6–17. [CrossRef]
8. Huang, T.; Yao, J.; Huang, Z.; Yin, X.; Xie, H.; Zhang, J. Numerical simulation on ferrofluid flow in fractured porous media based on discrete-fracture model. *Open Phys.* **2017**, *15*, 370–378. [CrossRef]
9. Neuringer, J.L. Some viscous flows of a saturated ferro-fluid under the combined influence of thermal and magnetic field gradients. *Intern. J. Non-Linear Mech.* **1966**, *1*, 123–137. [CrossRef]
10. Majeed, A.; Zeeshan, A.; Ellahi, R. Unsteady ferromagnetic liquid flow and heat transfer analysis over a stretching sheet with the effect of dipole and prescribed heat flux. *J. Mol. Liquids* **2016**, *223*, 528–533. [CrossRef]
11. Crane, L.J. Flow past a stretching plate. *J. Appl. Math. Phys.* **1970**, *21*, 645–647. [CrossRef]
12. Gupta, P.S.; Gupta, A.S. Heat and mass transfer on a stretching sheet with suction or blowing. *Can. J. Chem. Eng.* **1977**, *55*, 744–746. [CrossRef]
13. Chakrabarti, A.; Gupta, A.S. Hydromagnetic flow and heat transfer over a stretching sheet. *Q. Appl. Math.* **1979**, *37*, 73–78. [CrossRef]
14. Andersson, H.I.; Bech, K.H.; Dandapat, B.S. Magnetohydrodynamic flow of a power-law fluid over a stretching sheet. *Intern. J. Non-Linear Mech.* **1992**, *27*, 929–936. [CrossRef]
15. Hayat, T.; Muhammad, T.; Shehzad, S.A.; Alsaedi, A. An analytical solution for magnetohydrodynamic Oldroyd-B nanofluid flow induced by a stretching sheet with heat generation/absorption. *Intern. J. Therm. Sci.* **2017**, *111*, 274–288. [CrossRef]
16. Muhammad, N.; Nadeem, S.; Haq, R.U. Heat transport phenomenon in the ferromagnetic fluid over a stretching sheet with thermal stratification. *Results Phys.* **2017**, *7*, 854–861. [CrossRef]
17. Ramzan, M.; Yousaf, F. Boundary layer flow of three-dimensional viscoelastic nanofluid past a bi-directional stretching sheet with Newtonian heating. *AIP Adv.* **2015**, *5*, 057132. [CrossRef]
18. Hussain, T.; Shehzad, S.A.; Hayat, T.; Alsaedi, A.; Al-Solamy, F.; Ramzan, M. Radiative hydromagnetic flow of Jeffrey nanofluid by an exponentially stretching sheet. *PLoS ONE* **2014**, *9*, e103719. [CrossRef] [PubMed]
19. Goto, Y.; Kamebuchi, Y.; Hagio, T.; Kamimoto, Y.; Ichino, R.; Bessho, T. Electrodeposition of copper/carbonous nanomaterial composite coatings for heat-dissipation materials. *Coatings* **2017**, *8*, 5. [CrossRef]
20. Park, J.E.; Jang, Y.S.; Bae, T.S.; Lee, M.H. Multi-Walled carbon nanotube coating on alkali treated TiO_2 nanotubes surface for improvement of biocompatibility. *Coatings* **2018**, *8*, 159. [CrossRef]
21. Rivero, P.; Garcia, J.; Quintana, I.; Rodriguez, R. Design of nanostructured functional coatings by using wet-chemistry methods. *Coatings* **2018**, *8*, 76. [CrossRef]
22. Ramzan, M.; Bilal, M.; Chung, J.D.; Lu, D.C.; Farooq, U. Impact of generalized Fourier's and Fick's laws on MHD 3D second grade nanofluid flow with variable thermal conductivity and convective heat and mass conditions. *Phys. Fluids* **2017**, *29*, 093102. [CrossRef]

23. Sanni, K.M.; Asghar, S.; Jalil, M.; Okechi, N.F. Flow of viscous fluid along a nonlinearly stretching curved surface. *Results Phys.* **2017**, *7*, 1–4. [CrossRef]
24. Sajid, M.; Iqbal, S.A.; Naveed, M.; Abbas, Z. Joule heating and magnetohydrodynamic effects on ferrofluid (Fe_3O_4) flow in a semi-porous curved channel. *J. Mol. Liquids* **2016**, *222*, 1115–1120. [CrossRef]
25. Roşca, N.C.; Pop, I. Unsteady boundary layer flow over a permeable curved stretching/shrinking surface. *Eur. J. Mech. B Fluids* **2015**, *51*, 61–67. [CrossRef]
26. Imtiaz, M.; Hayat, T.; Alsaedi, A. Convective flow of ferrofluid due to a curved stretching surface with homogeneous-heterogeneous reactions. *Powder Technol.* **2017**, *310*, 154–162. [CrossRef]
27. Naveed, M.; Abbas, Z.; Sajid, M. MHD flow of micropolar fluid due to a curved stretching sheet with thermal radiation. *J. Appl. Fluid Mech.* **2016**, *9*, 131–138. [CrossRef]
28. Hone, J. Carbon nanotubes: Thermal properties. *Dekker Encycl. Nanosci. Nanotechnol.* **2004**, 603–610.
29. Antar, Z.; Noel, H.; Feller, J.F.; Glouannec, P.; Elleuch, K. Thermophysical and radiative properties of conductive biopolymer composite. *Mater. Sci. Forum* **2012**, *714*, 115–122. [CrossRef]
30. Oztop, H.F.; Abu-Nada, E. Numerical study of natural convection in partially heated rectangular enclosures filled with nanofluids. *Intern. J. Heat Fluid Flow* **2008**, *29*, 1326–1336. [CrossRef]
31. Ebrahimnia-Bajestan, E.; Niazmand, H. Convective heat transfer of nanofluids flows through an isothermally heated curved pipe. *Iran. J. Chem. Eng.* **2011**, *8*, 81–97.
32. Bejan, A. *Convection Heat Transfer*; John Wiley & Sons Inc.: Hoboken, NJ, USA, 2013.
33. Zhang, Y.; Shi, Q.; Schliesser, J.; Woodfield, B.F.; Nan, Z. Magnetic and thermodynamic properties of nanosized Zn ferrite with normal spinal structure synthesized using a facile method. *Inorg. Chem.* **2014**, *53*, 10463–10470. [CrossRef] [PubMed]
34. Khorasanizadeh, H.; Nikfar, M.; Amani, J. Entropy generation of Cu-water nanofluid mixed convection in a cavity. *Eur. J. Mech.* **2013**, *37*, 143–152. [CrossRef]



© 2018 by the authors. Licensee MDPI, Basel, Switzerland. This article is an open access article distributed under the terms and conditions of the Creative Commons Attribution (CC BY) license (http://creativecommons.org/licenses/by/4.0/).